Evaluation of the relevance of melt pool dynamics in Laser Material Deposition process modeling

CrossMark

Jon Iñaki Arrizubieta [a],*, Aitzol Lamikiz [a], Fritz Klocke [b], Silvia Martínez [a], Kristian Arntz [b], Eneko Ukar [a]

[a] Department of Mechanical Engineering, University of the Basque Country UPV/EHU, c/ Plaza Torres Quevedo 1, 48013 Bilbao, Spain
[b] Fraunhofer Institute for Production Technology IPT, Steinbachstrasse 17, 52074 Aachen, Germany

ABSTRACT

The melt pool dynamics consideration in the numeric modeling of the Laser Material Deposition (LMD) process can be enormously difficult and expensive, especially if this calculation is not strictly necessary. The increased cost comes mainly from the necessity of considering a higher number of input parameters into the model in addition to the computational cost. Therefore, an analysis of the influence of the melt pool dynamics in a LMD model and its impact on the accuracy is presented. For this purpose, a numeric model that simulates the melt pool fluid-dynamics has been developed and experimentally validated for different situations. After a detailed analysis of the results, an exponential formula based on the response surface methodology (RSM) that quantifies the influence of the fluid-dynamic phenomena inside the melt pool has been obtained. The main conclusion of the present work is that the LMD process can be addresses as a thermal problem without considering the melt pool dynamics and without losing accuracy for a certain window of process parameters, what reduces the computational cost and will allow an easier integration of the model in CAE tools for process simulation.

1. Introduction

The Laser Material Deposition (LMD) is an additive manufacturing process based on the generation of a melt pool on the surface of a substrate, while filler material is added in wire or powder form [1]. As the laser beam focusing position moves, the resulting combination of substrate and filler material solidifies almost instantly due to the high cooling rates, which values can be up to 10^3–10^5·K·s^{-1} [2], and consequently, high quality metallurgical bonding is obtained. The LMD process is gaining relevance in industry because of its advantages over other additive techniques such as arc welding or thermal spray [3]. Some authors ensure that the LMD process provides better quality coatings, together with a minimal dilution, minimal distortion and good surface quality [4]. Thanks to these advantages, as Wissenbach stated, LMD has become a reference technique in many companies for applying wear and corrosion protective layers on metallic workpieces as well as for the repair of high added value components [5].

Many authors have focused their efforts on modeling the LMD process and Pinkerton carried out a depth review of the most rel-

evant works in this field [6]. Regarding material addition, most authors assume the statement that all powder particles that fall inside the melt pool contribute to the clad generation [7,8]. In the same direction, the size of the melt pool is determined by the temperature field in the substrate and therefore the interaction between the laser beam and the substrate must be properly modeled in order to obtain an accurate LMD model [9]. Therefore, it is really important to model properly the interaction between the laser beam and the substrate [10].

Typically, with the aim of reducing the computational cost and facilitate the programing, the problem is addressed in a simplified way. Typical assumptions considered by different authors are the omission of the material displacement inside the melt pool [11–16], or the implementation of an enhanced thermal conductivity coefficient for the heat transfer inside the melt pool [17,18]. Even authors that consider the movement of the molten material introduce simplifications such as the supposition of a laminar flow with a viscous incompressible heat conducting fluid [19] or the assumption that the surface of the substrate remains flat and no interface movement occurs [20]. More complex models that include the movement of the molten material and the displacement of the surface interface have been presented [21,22] where the geometry of the melt pool is modeled with high accuracy.

However, it is difficult to quantify the impact of these assumptions on the accuracy of the resulting model. Moreover, most of

* Corresponding author at: Department of Mechanical Engineering, University of the Basque Country (UPV/EHU), Faculty of Engineering in Bilbao, c/Plaza Torres Quevedo 1, 48013 Bilbao, Spain.
E-mail address: joninaki.arrizubieta@ehu.eus (J.I. Arrizubieta).

Nomenclature

u	fluid velocity in the X axis direction	T	time variable
v	fluid velocity in the Y axis direction	Δt	time step
w	fluid velocity in the Z axis direction	t_{int}	powder particle - laser beam interaction time
U	absolute fluid velocity	P	laser power
Δx	element size in the X axis direction	P_{att}	laser power attenuation
Δy	element size in the Y axis direction	q_{laser}	laser beam intensity
Δz	element size in the Z axis direction	q_{losses}	energy losses due to radiation and convection
ρ	material density	r_l	laser beam radius in the focal plane
p	pressure value	α	absorptivity
μ	material viscosity	h	convection coefficient
$\underline{g}$	gravitational acceleration constant	ε	emissivity
$\vec{e}$	Z+ direction unitary vector	σ_b	Stefan-Boltzmann coefficient
γ	volume fraction (solid/liquid)	t_{int}	interaction time between laser beam and powder parti-
σ	surface tension		cles
$\frac{d\sigma}{dT}$	surface tension variation regarding the temperature	$L_{average}$	average distance that powder particles travel through
κ	surface curvature		the laser beam
$\vec{n}$	vector normal to the surface (solid/liquid – gas inter-	θ	laser beam semi-angle
	face)	δ	angle between the tangent of the surface and the hori-
β	coefficient of liquid thermal expansion		zontal
c	specific energy	fpp	focal plane position
L	latent heat of fusion	υ_p	powder particle average velocity at the nozzle exit
k	heat conductivity	r_{pm}	powder particle average radius
T	temperature	S_p	powder particle projected area
$T_{solidus}$	solidus temperature	m_p	powder particle average mass
$T_{liquidus}$	liquidus temperature	MP	melt pool fluid-dynamic relevance coefficient
T_∞	room temperature	I	laser beam average intensity
$T_{initial}$	powder particle preheating temperature	υ_f	LMD machine feed rate
T_p	temperature of the powder particles when they enter into the melt pool	$\dot{m}$	powder mass rate

LMD models do not implement melt-pool dynamics, but do not have evaluated neither the relevance of considering the melt pool fluid-dynamics, nor the impact of their omission in the accuracy of the model. On the other hand, if these fluid-dynamic phenomena are not considered, the resulting computational cost of the model is considerably reduced and this could enable their implementation in CAD/CAM/CAE tools [23]. Nevertheless, a sufficient level of accuracy must be also maintained.

Consequently, the present work focuses on the analysis of the relevance of considering or neglecting the melt pool fluid-dynamics in a LMD model and its influence on the accuracy of the numerical model. For this purpose, a series of experimental tests have been performed in order to validate the model and determine the influence of the movement of the molten material in the melt pool.

2. Methodology proposed to analyze the influence of the fluid-dynamic phenomena inside the melt pool

The used model has been entirely programmed in Matlab environment and the following deployed methodology has been applied for the analysis of the relevance of the fluid-dynamic phenomena inside the melt pool, see Fig. 1. First of all, a model that simulates the melt pool fluid-dynamic phenomena under a static laser beam has been developed based on the classic SIMPLE algorithm developed by Patankar [24].

Once the numerical model has been experimentally validated for simulating the melt pool under a static laser beam, the model has been adapted for simulating the full LMD process. The LMD model enables to simulate the material deposition under the consideration or the omission of the fluid-dynamic phenomena. Simultaneously, a series of experimental tests have been carried out in

order to validate the model and analyze its accuracy. Finally, an evaluation of the relevance of the melt pool fluid-dynamics on the LMD process is presented.

3. Description of the simulation model

As it has been mentioned in the previous section, the model has been developed in 3 steps: First, a model that simulates the melt pool dynamics under a static laser beam has been completed. Afterwards, a complete LMD model, including the melt pool dynamics consideration, has been performed. Finally, a simplified model of LMD process has been carried out, neglecting the effect of the fluid dynamics into de melt pool.

3.1. Melt pool dynamics governing equations

The proposed model is based on a classical solution, which solves continuity (2), momentum (3) and energy conservation (6) equations in order to obtain the pressure, velocity and temperature fields of each element respectively. Both, conduction and diffusion have been considered as heat transfer mechanisms inside the substrate. Furthermore, the Volume of Fluid (VOF) equation (9) has been solved in order to simulate the material flow inside the control volume and enable the liquid-gas boundary movement when the process requires it.

All the analyzed variables are assumed to have a linear variation during the time interval "Δt". Moreover, as it is shown in Eq. (1), a fully implicit scheme has been adopted ($f = 1$), this means that for each time step the value of the variable for the next time step is calculated.

$$\int_t^{t+\Delta t} \phi_P \cdot dt = [f \cdot \phi_P + (1-f) \cdot \phi_P^0] \cdot \Delta t = \phi_P \cdot \Delta t \qquad (1)$$
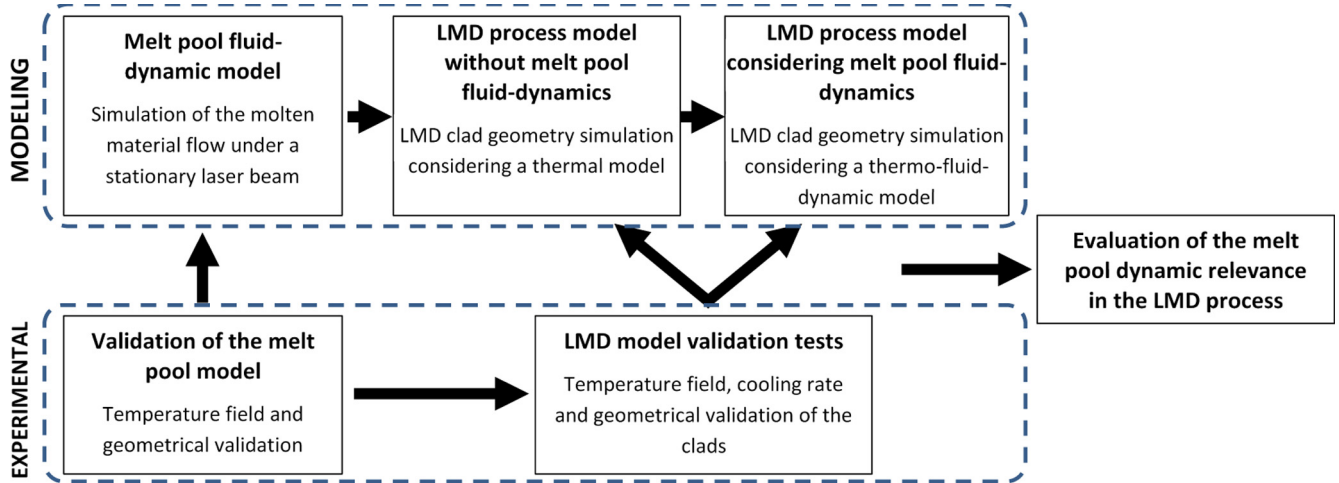
Fig. 1. Flowchart of the deployed methodology.

3.1.1. Continuity equation

$$\frac{\partial \rho}{\partial t} + \frac{\partial}{\partial x}(\rho \cdot u) + \frac{\partial}{\partial y}(\rho \cdot v) + \frac{\partial}{\partial z}(\rho \cdot w) = 0 \qquad (2)$$

It is assumed that the density "ρ" does not vary directly with the pressure and its value prevails in the whole mesh element. Besides, it is supposed that the velocities "u", "v" and "w" are constant in the whole element faces, in the X, Y and Z directions respectively.

3.1.2. Momentum conservation equation

$$\frac{\partial}{\partial t}(\rho \cdot \phi) + \frac{\partial}{\partial x}(\rho \cdot u \cdot \phi) + \frac{\partial}{\partial y}(\rho \cdot v \cdot \phi) + \frac{\partial}{\partial z}(\rho \cdot w \cdot \phi)$$
$$= -\frac{\partial p}{\partial x} + \frac{\partial}{\partial x}\left(\mu \cdot \frac{\partial \phi}{\partial x}\right) - \frac{\partial p}{\partial y} + \frac{\partial}{\partial y}\left(\mu \cdot \frac{\partial \phi}{\partial y}\right) - \frac{\partial p}{\partial z}$$
$$+ \frac{\partial}{\partial z}\left(\mu \cdot \frac{\partial \phi}{\partial z}\right) + S_m \qquad (3)$$

In Eq. (3) the variable "ϕ" stands for the relevant velocity component. The momentum generation term "S_m" can be split into two terms: On the one side, the buoyancy force generated as a consequence of the density difference, "S_b". On the other side, the velocity reduction term introduced in those elements where the material is in solid state "S_d". The assumption that the material is completely rigid and incompressible when becomes solid has been adopted; hence, the material has a zero velocity in the solid zone. The parameter "f_l" has a zero value in the solid and a unit value in the liquid. In order to avoid zeros in the denominator, $C = 10^6$ and $e_0 = 10^{-3}$ values have been adopted [24].

$$S_m = S_b + S_d = \rho \cdot g \cdot \beta \cdot (T - T_\infty) \cdot \vec{e} + A \cdot U \qquad (4)$$

$$S_m = \rho \cdot g \cdot \beta \cdot (T - T_\infty) \cdot \vec{e} - \frac{C \cdot (1 - f_l)}{f_l^3 + e_0} \cdot U \qquad (5)$$

3.1.3. Energy conservation equation

$$\frac{\partial}{\partial t}(\rho \cdot c \cdot T) + \frac{\partial}{\partial x}(\rho \cdot c \cdot u \cdot T) + \frac{\partial}{\partial y}(\rho \cdot c \cdot v \cdot T) + \frac{\partial}{\partial z}(\rho \cdot c \cdot w \cdot T)$$
$$= \frac{\partial}{\partial x}\left(k \cdot \frac{\partial T}{\partial x}\right) + \frac{\partial}{\partial y}\left(k \cdot \frac{\partial T}{\partial y}\right) + \frac{\partial}{\partial z}\left(k \cdot \frac{\partial T}{\partial z}\right) + S_e \qquad (6)$$

The energy generation term "S_e" is defined as it follows: "S_L" is the latent heat and "S_C" is the heat exchange at the substrate surface. Inside this second term, the energy introduced by the laser beam (q_{laser}) and the heat losses due to radiation and convection (q_{losses}) are included.

$$S_e = S_L + S_C \qquad (7)$$

In order to simplify the programming, the latent heat is defined by means of Eq. (8), where "$\partial L/\partial T$" represents the latent heat variation regarding the temperature and "$\partial T/\partial t$" is the temperature variation between two successive time steps.

$$S_L = \rho \cdot \frac{\partial L}{\partial t} = \rho \cdot \frac{\partial L}{\partial T} \cdot \frac{\partial T}{\partial t} \qquad (8)$$

3.1.4. VOF (Volume of Fluid) equation

In the simulations where different phases coexist, one of the most challenging tasks is to determine the position and shape of the interface surface. In the present work, the interface capturing method has been used for tracking the free interface. The reason for choosing this method is the fact that it does not introduce any restrictions to the interface evolution. As it is shown in Eq. (9), a scalar transport variable (γ) that determines the boundary between the different phases and describes the evolution of the interface as a solution to the mass transfer equation has been defined.

$$\frac{\partial \gamma}{\partial t} + \nabla(\gamma \cdot U) = 0 \qquad (9)$$

The volume fraction "γ" becomes a zero value in the gas and a unit value in the base material (solid or liquid). The interface is defined as the transition zone where "γ" takes a value between 0 and 1.

3.1.5. SIMPLE algorithm and staggered grid

The SIMPLE algorithm proposed by Patankar [24] has been used to solve the coupled pressure-velocity equations. Thus, by means of the usage of two different grids, these difficulties have been overcome: A conventional grid has been used for all the variables; whereas a staggered grid has been used for the velocities.

3.1.6. Initial conditions

At the initial time step the modeled geometry is supposed to be at room temperature (T_∞ = 298 K). Therefore, the substrate and powder are in solid state and all the elements have a zero velocity

value. Moreover, an initial condition of zero velocity in the gas layers above the surface of the part is supposed.

3.1.7. Boundary conditions

A zero pressure gradient condition has been stablished in all the boundaries of the developed model. The model works with relative pressures and therefore, once the pressure field is calculated the lower pressure value is equaled to zero. This way, all the pressures are positive and overflow problems are avoided. Moreover, a "zero velocity variation" condition has been stablished in all boundary faces (see Fig. 2).

In terms of the temperature boundaries, the nodes next to the control volume are forced to be at room temperature (T_∞ = 298 K). This is the same as imposing a first specie or Dirichlet boundary condition, Eq. (10).

$$q = k \cdot \left(\frac{\partial T}{\partial x} + \frac{\partial T}{\partial y} + \frac{\partial T}{\partial z} \right) \tag{10}$$

Lastly, with the aim of reducing unnecessary computational cost and based on the symmetric nature of the modeled problem, just half of the volume has been simulated. The following boundary conditions have been stablished in the symmetry plane:

$$\frac{dT}{dy} = 0; \quad v = 0; \quad \frac{du}{dy} = 0; \quad \frac{dw}{dy} = 0 \tag{11}$$

3.1.8. Heat source modeling

Inside the heat exchange term at the surface of the substrate "S_C" in Eq. (7), the energy introduced by the laser beam into the system (q_{laser}) and the radiation and convection losses (q_{losses}) are included. The laser beam is considered to have a Gaussian energy distribution, where "r_l" is the beam radius at the surface of the substrate. Therefore, the energy density that the laser beam introduces in a determined point at the surface of the substrate can be calculated by means of Eq. (12), where "x" and "y" define the planar distance between that point and the center of the laser beam. As the free surface can deform freely, the absorptivity value "α" is modified as a function of the angle between the horizontal and the tangent of the free surface "δ".

$$q_{laser} = \frac{2 \cdot \alpha \cdot \cos(\delta) \cdot P}{\pi \cdot r_l^2} \cdot e^{-2 \cdot \left(\frac{x^2 + y^2}{r_l^2} \right)} \tag{12}$$
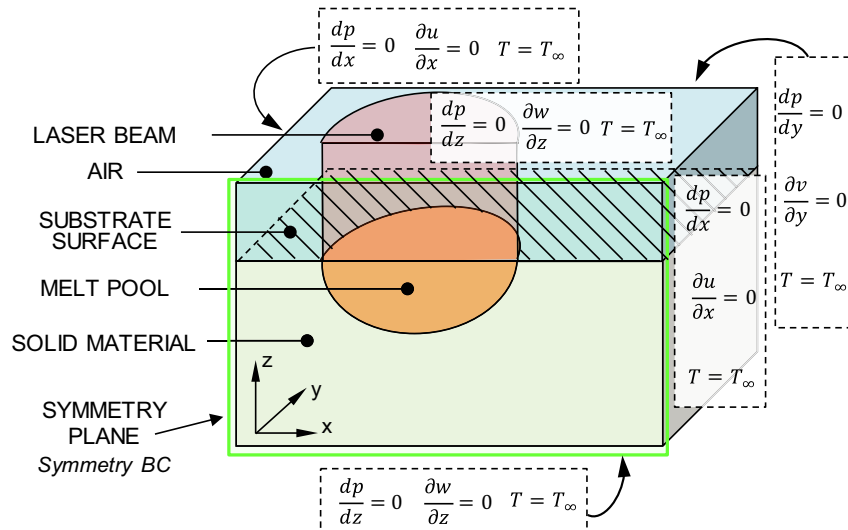
Radiation and convection losses at the surface of the substrate are described by Eq. (13).

$$q_{losses} = h \cdot (T - T_\infty) + \varepsilon \cdot \sigma_b \cdot (T^4 - T_\infty^4) \tag{13}$$

3.1.9. Surface forces

Two surface forces have been included in the present numerical model: On the one hand, a surface force generated as a consequence of the curvature developed by the interface between the air and the substrate "$f_{S,n}$"; this force has a normal direction to the surface. On the other hand, as a consequence of the surface stress variation regarding the temperature variation, Marangoni stresses are generated on the surface of the molten material and they induce tangential forces on the surface "$f_{S,t}$". A scheme of the surface forces is shown in Fig. 3.

$$f_S = f_{S,n} + f_{S,t} = \sigma \cdot \kappa \cdot \vec{n} + \nabla_t \sigma \tag{14}$$

The vector normal to the surface is defined by means of Eq. (15) and the gradient tangential operation is defined by means of Eq. (16). The term "$d\sigma/dT$" represents the material surface tension variation regarding the temperature and it is related with the Marangoni stresses.

$$\vec{n} = \frac{\nabla \gamma}{|\nabla \gamma|} = \frac{\frac{\partial \gamma}{\partial x} + \frac{\partial \gamma}{\partial y}}{\left| \frac{\partial \gamma}{\partial x} + \frac{\partial \gamma}{\partial y} \right|} \tag{15}$$

$$\nabla_t \sigma = \frac{d\sigma}{dT} \nabla_t T = \frac{d\sigma}{dT} \frac{\partial T}{\partial \vec{t}} = \frac{d\sigma}{dT} [\nabla T - \vec{n} \cdot (\vec{n} \cdot \nabla T)] \tag{16}$$
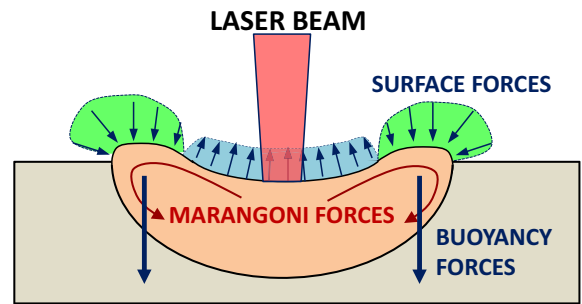

Fig. 3. Surface forces and the buoyancy force.

Fig. 2. Applied boundary conditions for modeling the melt pool under a static laser beam.

Combining previous Eqs. (14)–(16), the following Eq. (17) that defines the surface forces acting in the interface between the substrate and the air is defined. At the end of Eq. (17) a term to avoid spurious currents and redistribute the forces in the highest density phase has been included [20]. The terms "ρ_1" and "ρ_2" are the densities of the substrate and air respectively.

$$f_S = \left[\sigma \cdot \kappa \cdot \vec{n} + \frac{d\sigma}{dT} [\nabla T - \vec{n} \cdot (\vec{n} \cdot \nabla T)] \right] \cdot \frac{2 \cdot \rho}{(\rho_1 + \rho_2)} \qquad (17)$$

3.2. LMD model considering melt pool dynamics

Once the melt pool fluid-dynamics model has been developed for a static laser no filler material, it is implemented in a complete LMD model. Besides the previously described equations, this model considers the interaction between the laser and the powder particles before being deposited, the heating of the substrate, the addition of filler material and, finally, the generation of the clad.

3.2.1. Laser beam and powder particle interaction

One of the most important steps in the LMD process is the injection of previously heated particles in the melt pool. The heating of the particles occurs above the melt pool, between the nozzle tip and the surface of the substrate, and it is generated because of the interaction between the powder particles and the laser beam. As a consequence of this interaction, two significant effects need to be considered: First, the laser beam is attenuated and the laser power that radiates the substrate is lower than the programmed value. Second, the powder particles are heated before they reach the melt pool.

As far as the powder drag gas and protective gas flows are set to a fixed value and remain constant, the powder distribution at the nozzle exit does not vary. Therefore, powder distribution at the nozzle exit can be considered as a constant input parameter for the LMD process model. The concentration of the powder particles has been calculated using the CFD program Fluent from Ansys and based on previously presented works [25]. As a result of this evaluation, a $1.38 \ \mathrm{m \cdot s^{-1}}$ average velocity of the powder particles at the nozzle exit has been estimated.

The laser beam attenuation has a direct impact on the LMD process and therefore it has been calculated. The attenuation model used in the present work is based on the shadow model developed by Tabernero et al. [26].

3.2.2. Inflight particle heating

As it has been previously stated, powder particles attenuate the laser beam but they also get heated during the interaction with the laser beam. Consequently, the powder particles that reach the surface of the substrate situated below the nozzle exit are heated or even melted depending on the laser power. In Fig. 4 a thermal image of the powder particles heated by a laser beam is shown.

With the aim of predicting the temperature of the powder particles when they are injected into the melt pool, a model based on the following assumptions has been developed:

1. All powder particles have the same velocity when they exit the nozzle.
2. The particle interaction time "t_{int}" is defined as a function of the average distance "$L_{average}$" that powder particles travel through the laser beam and the "v_p" particle average velocity. The distance "$L_{average}$" is determined based on the geometrical relations from Fig. 4. Therefore, the interaction time can be defined as it follows:

$$t_{int} = \frac{L_{average}}{v_p} = \frac{\frac{\sin(90+\theta)}{\sin(20°)} \cdot r_l}{v_p} \qquad (18)$$

3. In the present model it is assumed that all particles have a constant diameter equal to the average diameter. The projected surface area and mass of the particles are defined as it follows:

$$S_p = \pi \cdot (r_{pm})^2 \qquad (19)$$

$$m_p = \rho \cdot \frac{4}{3} \cdot \pi \cdot (r_{pm})^3 \qquad (20)$$

4. Since the diameter of the particles is lower than 125 μm, the mass of the particle is very low and it can be assumed that the temperature in the whole particle is constant.

Powder feeders usually include a heating system to eliminate the moisture from the powder particles and the initial temperature "$T_{initial}$" is higher than the room temperature. Therefore, the temperature that the powder particles reach when they are introduced into the melt pool is defined as it follows:

$$\begin{cases} T_p = T_{initial} + \frac{\alpha \cdot P \cdot t_{int}}{\pi \cdot (r_l)^2} \cdot \frac{S_p}{c \cdot m_p}; & \text{if } T < T_{fusi} \\ T_p = T_{initial} + \left[\frac{\alpha \cdot P \cdot t_{int} \cdot S_p}{\pi \cdot (r_l)^2} - \frac{L \cdot (T - T_{fusi})}{(T_{fusf} - T_{fusi})} \cdot m_p \right] \cdot \frac{1}{c \cdot m_p}; & \text{if } T_{fusi} \leqslant T < T_{fusf} \\ T_p = T_{initial} + \left[\frac{\alpha \cdot P \cdot t_{int} \cdot S_p}{\pi \cdot (r_l)^2} - L \cdot m_p \right] \cdot \frac{1}{c \cdot m_p}; & \text{if } T \geqslant T_{fusf} \end{cases} \qquad (21)$$

3.2.3. Clad generation

Once the laser beam generates a melt pool in the substrate, filler material is added at a programmed mass rate. The concentration of the powder particles follows a Gaussian distribution at the focal plane [25], with a maximum concentration at the axis center. The model supposes that powder particles are trapped when they fall inside the melt pool and lost when they fall outside and find solid substrate material. When the filler material fills a cell, this cell changes its state from gas to liquid or solid (depending on the temperature reached by the powder particles as a consequence of their heating during the inflight time). As it has been justified before, the interface capturing method has been used for tracking the motion of the free interface.

Thus, when the filler material is added to the substrate, both material and energy are introduced to the substrate. Once the material is added, it becomes part of the substrate and behaves according to the equations described at the Section 3.1 (see Fig. 5).

3.3. LMD model without considering melt pool dynamics

In this third case, the LMD model works directly as a conventional thermal model, where filler material is added to the substrate. Since the objective of the research work is to quantify the relevance of the molten material displacement in the LMD process, same considerations as in the previous case have been taken into account for the powder flow, the interaction between the laser beam and the powder particles during the inflight time and the criteria for the trapped powder on the substrate.

Conduction has been considered as the only heat transfer mechanism inside the workpiece and melt pool fluid-dynamic phenomena have been completely omitted. In addition, no conductivity enhancement factors have been used. Therefore, the simplified model presents a much lower computational cost and simulation times are reduced considerably in comparison with the full model.

The usage of experimentally defined conductivity enhancement factors can improve considerably the accuracy of the thermal
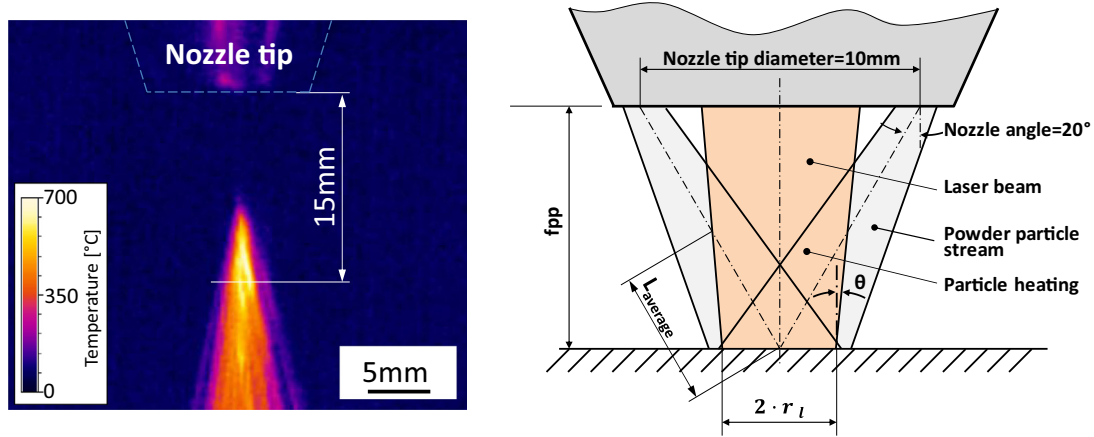
Fig. 4. Thermal image of the heated powder particles at the nozzle exit for a 1000 W laser power (left) and geometric relations (right).
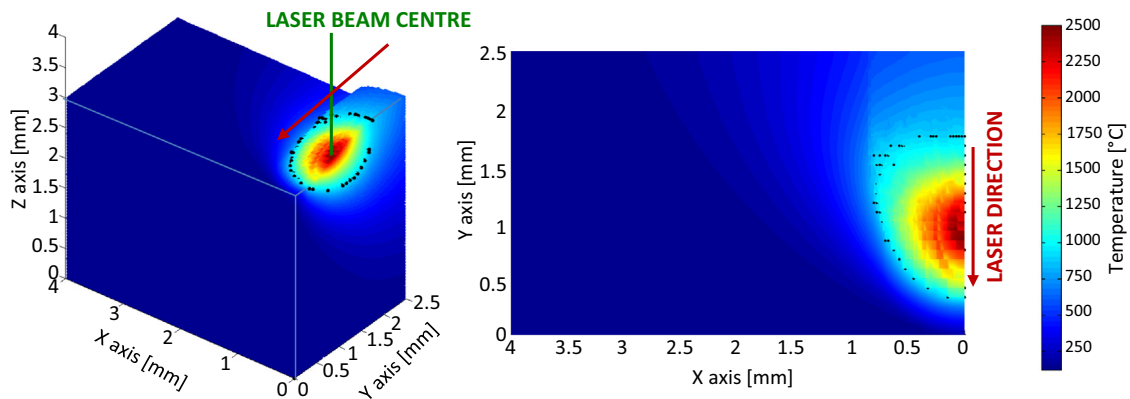

Fig. 5. 3D simulation of a LMD test considering fluid-dynamic phenomena inside the melt pool. Process parameters: P = 800 W, v_f = 500 mm/min, $\dot{m}$ = 4 g·min^{-1}.

model. However, they would also falsify the results, because more variables rather than the melt-pool dynamics would be changed between the different models. Therefore, none of them is decided to be included.

4. Experimental validation of the influence of the melt pool dynamics in the LMD process

In order to validate experimentally the proposed methodology, an AISI 304 stainless steel has been used as substrate material. The material properties are detailed in Table 1, whereas, the composition is shown in Table 2.

4.1. Analysis of the melt pool generated by a stationary laser beam

First of all, different cross sections of the melt pool generated by a stationary laser beam have been analyzed considering the effect of the melt-pool dynamics. The model has been solved using a finite differences algorithm and, in order to obtain a high accuracy, a constant 25 μm element size and a 1×10^{-4} s time step have been stablished for validating the model. A 10^{-4} residue value has been defined between two iterations for mass, momentum, energy conservation and VOF equations to guarantee the convergence of the results. In all simulations a constant 25 °C room temperature has been supposed. Based on the results obtained by Saldi et al., who demonstrated the importance of the cooling process in the final shape of the melt pool, an extra time has been simulated after the laser is turned off in order to analyze the cooling stage [20].

Table 1
AISI 304 properties [27].

Material	AISI 304	
Density: ρ	7200	[kg·m^{-3}]
Specific energy (20 °C): c	760	[J·kg^{-1}·K^{-1}]
Solidus temperature: T$_{solidus}$	1697	[K]
Liquidus temperature: T$_{liquidus}$	1727	[K]
Latent heat of fusion: L	$6.0 \cdot 10^4$	[J·kg^{-1}]
Coefficient of liquid thermal expansion: β	$1.96 \cdot 10^{-5}$	[K^{-1}]
Conductivity: k	16.2	[W·m^{-1}·K^{-1}]
Liquid conductivity: k	35	[W·m^{-1}·K^{-1}]
Dynamic viscosity: μ	0.006	[N·m^{-2}·s]
Material absorptivity: α	0.3	[-]
Material emissivity: ε	0.3	[-]
Convection coefficient: h	20	[W·m^{-2}·K^{-1}]
Surface tension: σ	1	[N·m^{-1}]
Surface tension variation: $\frac{d\sigma}{dT}$	$-0.43 \cdot 10^{-4}$	[N·m^{-1}·K^{-1}]

A Rofin FL010 fiber laser with a 1 kW maximum power has been used for the experimental tests. The laser beam has been slightly defocused until a 2.5 mm spot diameter is obtained at the working plane. With the aim of analyzing all possible situations, different laser powers (ranging 250–1000 W) and interaction times (0.2–4 s) have been combined. During the tests, the temperatures reached in the melt pool have been measured using a two-color pyrometer. Besides obtaining the value of the maximum temperature reached in the melt pool, it helps when determining whether plasma is generated or not. Plasma generation is detected because it produces instabilities in the measured temperatures. In Fig. 6, the temperature measurements of two laser pulses are shown,

Table 2
AISI 304 composition (data from *ASM Aerospace Specification Metals, Inc.*).

Component	C	Cr	Fe	Mn	Ni	P	S	Si
Wt [%]	≤0.08	18–20	Balance	≤2	8–10.5	≤0.045	≤0.03	≤1
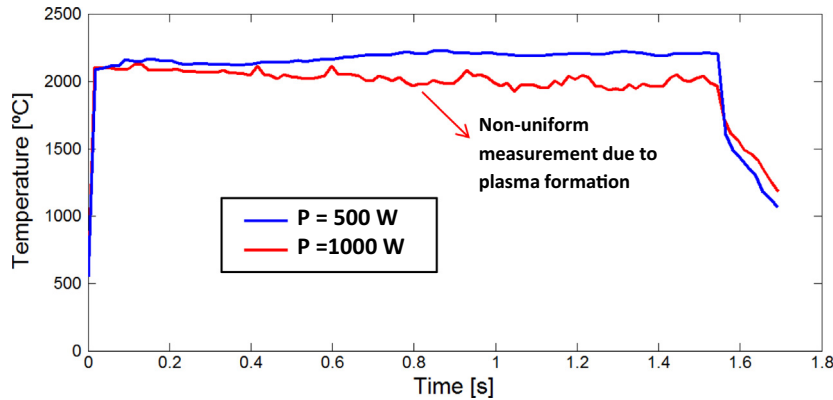
Fig. 6. Melt pool temperature measurements by means of a two-color pyrometer. (For interpretation of the references to colour in this figure legend, the reader is referred to the web version of this article.)

both pulses have a 1.5 s duration. In the case of using a 500 W laser power, a steady temperature measurement has been obtained; whereas in the case of 1000 W, plasma has been generated and the melt pool temperature measurement resulted to be unstable.

Plasma generation generates a decreasing maximum temperature inside the melt pool. The higher the laser power, the higher the temperature variations. For the AISI 304 base material and a fiber laser it is concluded that plasma is generated for laser energy densities above $5.6 \cdot 10^5$ J·m^{-2}.

In Table 3, the process conditions of the different tests are detailed together with the diameter of the generated melt pool. Since the developed model does not consider the generation of plasma, the working window where plasma is generated has been

avoided. "NM" indicates that the material has not been melted by the laser beam and "PG" shows that plasma has been generated. In both cases no values of the generated melt pool size have been reported.

With the aim of validating the developed model, the different experimental tests have been simulated (see Fig. 7). As an example, the results of the comparison of two tests are shown in Table 4. Once the experimentally generated melt pools have solidified, both tests have been cross sectioned, polished and etched. The melt pool width and depth have been measured in order to compare the experimental results with those predicted by the model. Moreover, the height reached as a consequence of the outward material flow has been measured. In all cases an absolute error lower than 0.1

Table 3
Conditions of the different stationary tests and the diameter of the generated crater.

[W]	$I_{average}$ [W·mm^{-2}]	Time [s]								
		0.2	0.4	0.6	0.8	1	1.5	2	3	4
1000	$2.04 \cdot 10^2$	1.451	1.647	3.043	3.222	PG	PG	PG	PG	PG
750	$1.53 \cdot 10^2$	1.282	1.426	2.802	2.841	3.160	PG	PG	PG	PG
500	$1.02 \cdot 10^2$	NM	1.176	2.008	2.145	2.288	3.072	3.022	PG	PG
250	$5.09 \cdot 10^1$	NM	NM	NM	NM	NM	NM	1.064	1.510	1.820
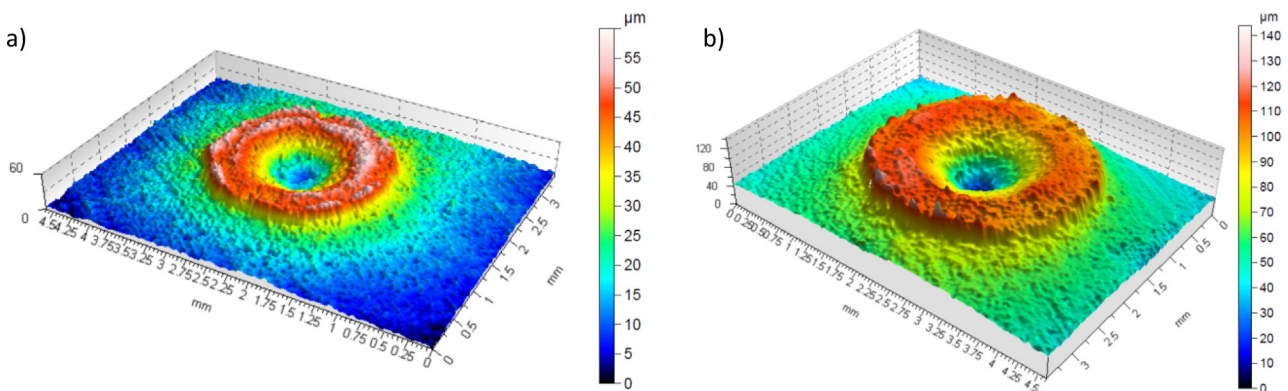
Fig. 7. Different topographies of the generated craters after the melt pool solidification. (a) P = 500 W, t = 0.6 s; (b) P = 750 W, t = 1 s.

Table 4
Dimensions of a crater generated under a stationary laser beam.

Test n°	P [W]	t [s]	Width [mm]		Depth [mm]		Height [mm]	
			Real	Model	Real	Model	Real	Model
1	500	1	2.288	2.225	0.352	0.355	0.063	0.050
2	750	0.6	2.802	2.850	0.962	0.925	0.060	0.050
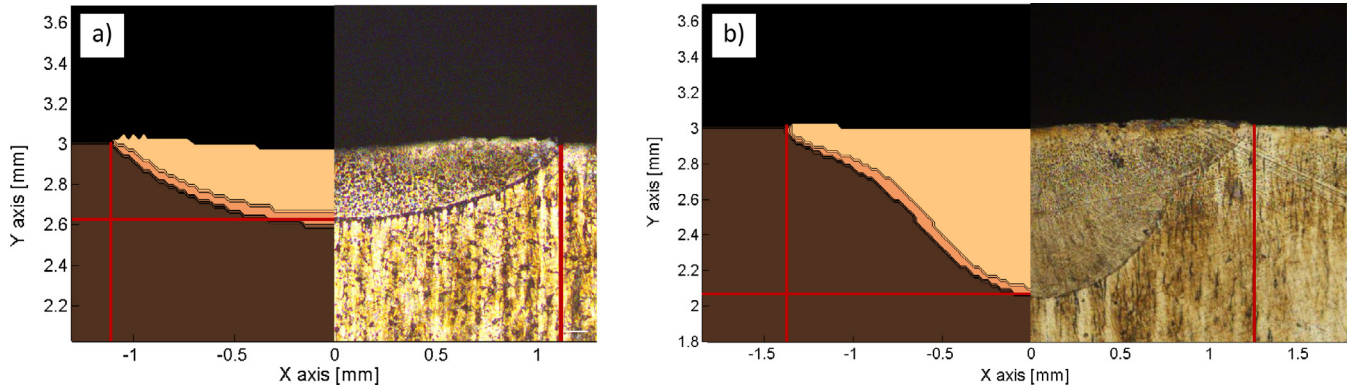
Fig. 8. Comparison between simulated and experimental melt pool cross sections. (a) Test 1: P = 500 W, t = 1 s; (b) Test 2: P = 750 W, t = 0.6 s.

mm has been obtained. The validation between the estimated and real dimensions of the melt pool is shown in Fig. 8.

As it can be seen in Fig. 8, material flow inside the melt pool plays a relevant role in its final shape. Higher laser intensities generate higher temperature gradients in the substrate; therefore conduction has a higher influence in the heat transfer mechanism and deeper melt pools are obtained.

In order to analyze the importance of the material flow in the final shape of the melt pool, simulation 1 has been repeated, but without considering the displacement of the material. Therefore, the heat conduction is the only heat transfer mechanism considered in the numerical model. This simulation without melt pool dynamic considerations has been named as 1′. The test conditions and obtained results are presented in Table 5, whereas the geometrical differences of the generated melt pool are shown in Fig. 9.

Table 5
Influence of the movement of the molten material in the geometry of the melt pool.

Test n°	P [W]	t [s]	Width [mm]	Depth [mm]	Height [mm]
1	500	1	2.225	0.355	0.050
1′	500	1	1.450	0.650	0
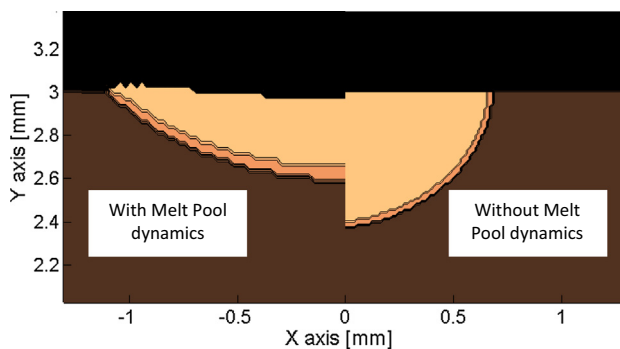
Fig. 9. Comparison between the cross sections of the test 1 (P = 500 W, t = 1 s) when material displacement is allowed (left) and when no material movement is allowed (right).

The molten material flow inside the melt pool not only influences its final geometry, since it also affects to the reached maximum temperatures. An outward material flow implies taking heat from the center of the melt pool and consequently the reached maximum temperature is lowered. In Fig. 10 a comparison between the maximum temperatures reached in both cases is shown. On the one hand, if no material displacement is considered, a maximum temperature of 3952 °C has been obtained. On the other hand, if melt pool fluid-dynamics are considered a much lower maximum temperature has been obtained, 2066 °C, which is much closer to the real measured temperature of 2107 °C. Therefore, it can be concluded that the geometry of the melt pool and its temperature field depend strongly on the developed velocity field.

4.2. Analysis of the clad generation in the LMD process

Once the developed model has been experimentally validated for predicting the geometry and the thermal field of the melt pool, it has been applied to estimate the geometry of the clad in the LMD process. The numerical model simulates the thermal field and material displacement while filler material is added into the substrate.

4.2.1. Powder particle heating

First of all, the average temperature reached by the powder particles when they are introduced into the melt pool has been calculated. The powder spot size has been modified and set to a 0.75 mm spot radius at the surface of the substrate and the focal plane position is fixed at 15 mm from the nozzle tip. Table 6 presents the input values for the particle heating model, Eq. (21), in order to calculate the temperature increase of the particles. Powder particles would heat up to the temperature values described in Table 7 when they reach the surface of the substrate.

The results of the model have been validated using a thermographic camera, which has been calibrated previously by means of a two-color pyrometer. As it can be seen in Table 7, an error below the 7% is obtained and therefore it is concluded that the inflight particle heating model works properly. Hereafter the results of the powder particle heating model are used in the LMD model.
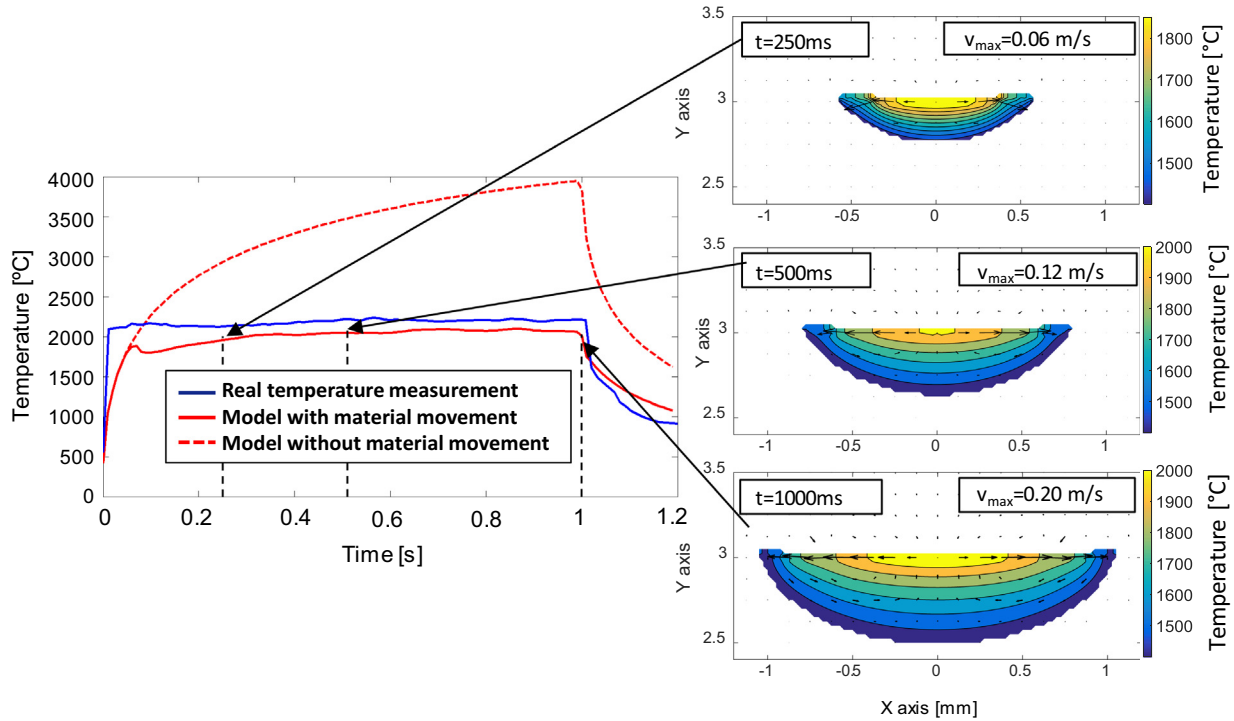
Fig. 10. (a) Comparison between the maximum temperatures reached for the test 1 and 1′; (b) evolution of the velocity and temperature fields during the test 1 (P = 500 W).

Table 6
Variable values for the powder particle heating model.

Variable	Symbol	Value
Travelled distance	$L_{average}$	2.193 mm
Laser beam radius	r_l	0.75 mm
Particle average velocity	v_p	1.38 m·s^{-1}
Particle radius	r_{pm}	$4.50 \cdot 10^{-5}$ m
Powder preheat	$T_{initial}$	60 °C

Table 7
Validation of the inflight particle heating model.

Laser power [W]	Temperature of powder particles at the focal plane		
	Real [°C]	Model [°C]	Error [%]
500	321.22	343.50	6.94
800	488.61	512.60	5.11
1000	608.81	627.00	2.99

Table 8
LMD conditions for validating the developed model.

Line	P [W]	v_f [mm·min^{-1}]	$\dot{m}$ [g·min^{-1}]	P_{att} [%]	T_p [°C]
1	500	500	2	7.2	343.50
2	500	1000	2	7.2	343.50
3	800	500	4	13.7	512.60
4	800	1000	4	13.8	512.60
5	1000	500	6	20.1	627.00
6	1000	1000	6	20.1	627.00

filled with material and deactivates them when there is no material. Consequently, as a 25 μm grid size has been used, the resolution of the simulated clad geometry is limited to this value and the model is not able to detect smaller geometry variations (see Table 9 and Fig. 11).

4.3. Influence of the melt pool dynamics in the LMD process

Based on the work carried out by Onwubolu et al. [28], an exponential model has been decided to be the most appropriate for determining the relevance of the melt pool dynamics. The clad height is the more sensitive variable regarding the melt pool dynamics and therefore, the error when predicting the clad height has been analyzed in Eq. (22). In this equation, the most relevant parameters that influence the process have been considered: the laser beam intensity (I), the amount of time in which a determined point of the substrate is under the laser beam (t) and the powder mass flow rate (m). It must be noticed that the time (t) is defined as the ratio between the laser beam diameter and the machine feed rate.

$$H = K \cdot I^k \cdot t^m \cdot (1 + \dot{m})^n = K \cdot I^k \cdot \left(\frac{2 \cdot r_l}{v_f} \right)^m \cdot (1 + \dot{m})^n \quad (22)$$

4.2.2. Design of the experimental tests

Six different clads have been deposited varying the laser power "P", machine feed rate "v_f" and the powder mass rate "$\dot{m}$". Powder has been delivered by a Sulzer Metco Twin 10-C powder feeder and injected into the processing area through a coaxial continuous nozzle. Powder attenuation "P_{att}", has been defined by means of the shadow model described in the Section 3.2.1 and the temperature of the powder particles when they enter into the melt pool "T_p" is defined by means of Eq. (21) (see Table 8).

4.2.3. Experimental test results

With the aim of validating the developed model, the geometry of the deposited clad has been measured. The total-height of the generated clad, defined as the sum of the clad height and depth, has been calculated in order to compare the experimental and simulated values. The model activates the grid elements when they are

Table 9
Comparison between the experimental and simulated geometry of the clads.

Line	Height [mm]			Height + Depth [mm]			Width [mm]		
	Real	Simulation	Error [%]	Real	Simulation	Error [%]	Real	Simulation	Error [%]
1	0.215	0.200	6.98	0.583	0.550	5.66	1.211	1.300	−7.35
2	0.080	0.075	6.25	0.282	0.300	−6.38	0.977	1.000	−2.35
3	0.354	0.350	1.13	0.936	0.850	9.19	1.663	1.700	−2.22
4	0.182	0.200	−9.89	0.614	0.550	6.35	1.351	1.250	7.48
5	0.484	0.500	−3.31	0.992	0.975	1.71	1.869	2.000	−7.01
6	0.283	0.300	−6.01	0.717	0.650	9.34	1.441	1.350	6.32
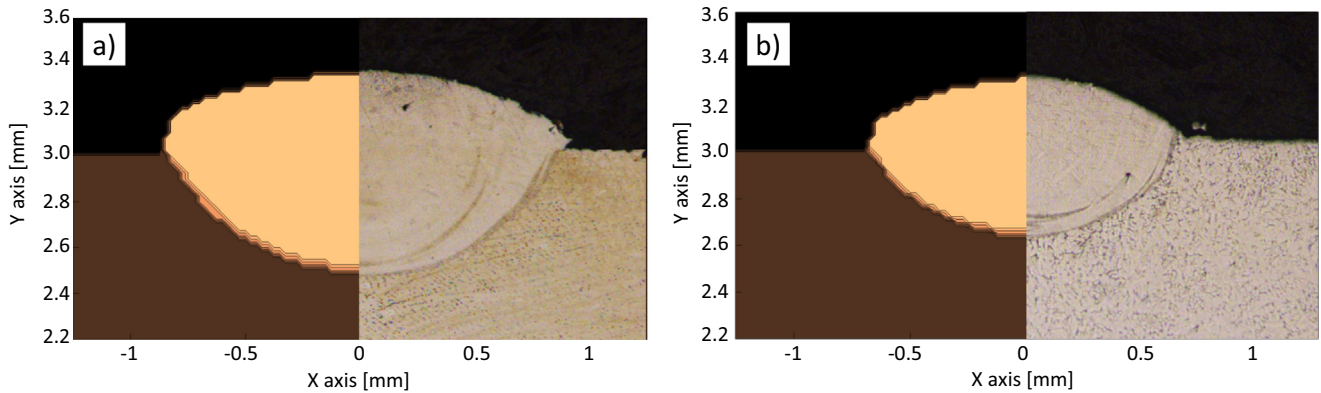
Fig. 11. Comparison between the simulated and experimental cross sections of the clad for (a) Line 3 and (b) Line 6.

When an error of the clad-height equal or below 0.025 mm is obtained, it has been supposed that there is no difference between the cases where the melt pool dynamics have been considered or omitted. The coefficient "K" has been modified in order to normalize the obtained results. Therefore, when the value of MP is below the unit, there is almost no difference between the cases where the fluid dynamics have been considered or omitted. The coefficients C, k, l, m are model parameters and they have been determined using the data from the model: C = $1.667 \cdot 10^{-4}$, k = 2, m = 1 and n = −1.

$$MP = C \cdot I^k \cdot t^m \cdot (1 + \dot{m})^n \qquad (23)$$

In the LMD process, filler material is constantly being added into the melt pool and, consequently as the substrate geometry is growing, the free surface is moving. Nevertheless, the surface does not move as in the case of the melt pool under a stationary laser beam; in the case of the LMD process new material is being added. Therefore, the influence of the Marangoni forces in the LMD process can be concluded to be minimal. This statement has been validated based on experimental measurements, where the temperature of the particles when they reach the melt pool has been measured. As the temperature of the particles is lower than the temperature of the material inside the melt pool, they minimize the existing temperature gradients and so happens with the Marangoni forces.

Furthermore, since the thermal cycle inside the LMD process is relatively fast, the laser beam goes over a certain point on the surface of the substrate in less than 0.2 s. Consequently, the influence of gravity on the movement of the molten material can be also neglected and the process could be simulated with relatively high accuracy without considering the fluid-dynamic phenomena of the molten material. Table 10 shows the comparison between the obtained results with and without melt pool fluid-dynamic consideration.

The value of the variable MP predicts the influence of the molten material displacement on the final dimensions of the deposited clad. In cases where the LMD process has a value of MP < 1 resulted that there is almost no difference in the dimensions of the clads between the numeric simulations where the fluid-dynamic phenomena have been considered or neglected. On the contrary, for MP values higher than the unit, the influence of the material displacement is increased and considerable differences are obtained in the geometry of the deposited clads.

Thus, based on the obtained results, it can be concluded that the LMD process can be modeled without considering melt pool fluid-dynamics phenomena with reasonably good accuracy for values of MP < 1. For instance, in Fig. 12 the cross sections of the deposited lines 4 and 5 are shown. As it can be seen, there is almost no difference regarding the clad geometry in Line 4 when fluid-
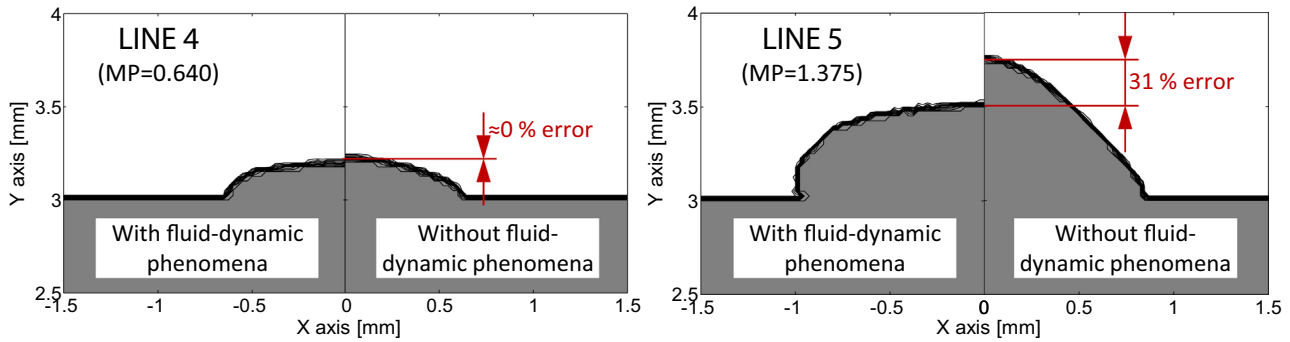
Table 10
Influence of the material displacement in the final geometry of the deposited clad.

Line	Height [mm]		Height + Depth [mm]		Width [mm]		MP
	With melt pool dynamics	Without melt pool dynamics	With melt pool dynamics	Without melt pool dynamics	With melt pool dynamics	Without melt pool dynamics	
1	0.200	0.200	0.550	0.550	1.300	1.300	0.775
2	0.075	0.100	0.300	0.325	1.000	1.000	0.390
3	0.350	0.450	0.850	0.950	1.700	1.550	1.280
4	0.200	0.200	0.550	0.550	1.250	1.200	0.640
5	0.500	0.725	0.975	1.200	2.000	1.650	1.375
6	0.300	0.325	0.650	0.675	1.350	1.300	0.685

Fig. 12. Relevance of the fluid-dynamic phenomena consideration in the LMD process.

Table 11
Influence of the material displacement in the cooling rate.

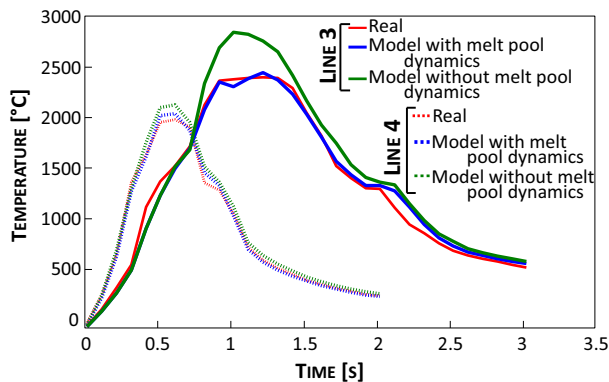| Line number	Real cooling rate [°C·s^{-1}]	Simulated cooling rates [°C·s^{-1}]			
		With movement	Error [%]	Without movement	Error [%]
1	−9842	−9841	−0.01	−9975	1.35
2	−11810	−10783	−8.69	−11775	−0.30
3	−6203	−5908	−4.75	−5555	−10.45
4	−7320	−7311	−0.12	−7614	4.03
5	−4054	−3800	−6.26	−5183	27.86
6	−6486	−6595	1.68	−6910	6.54

Fig. 13. Comparison between the cooling rates for lines 3 and 4 (*Line 3*: P = 800 W, v_f = 500 mm·min^{-1}, $\dot{m}$ = 4 g·min^{-1}; *Line 4*: P = 800 W, v_f = 1000 mm·min^{-1}, $\dot{m}$ = 4 g·min^{-1}).

dynamic phenomena are considered or omitted. However, a considerable difference can be observed in Line 5, where the MP coefficient is higher than the unit.

Besides the final geometry of the clad, the maximum temperatures and cooling rates have been evaluated. In Table 11 the real and simulated cooling rates are compared. As it can be seen, for lines 3 and 5 where the MP coefficient value is higher, a higher deviation is obtained, whereas for MP values below the unit almost no difference is obtained.

In Fig. 13 the evolution of the temperature of a specific point on the surface of the substrate that the laser goes over is shown. In Line 4 there is almost no difference between the real and modeled cases. However, if no melt pool fluid-dynamics are considered in Line 3, the modeled results are far from the real ones.

5. Conclusions

In the present paper, an evaluation of the relevance of the melt pool fluid-dynamics in the LMD process has been carried out, both

experimentally and theoretically. Based on the obtained results, the influence of omitting the melt pool fluid-dynamics on the LMD process has been analyzed and a process window where this assumption is valid has been determined and justified. The following conclusions have been reached after the realization of the present study:

- A model that considers the molten material movement and the heat transfer inside the substrate has been developed. This model resulted capable of predicting the geometry of the deposited clad in the LMD process with an error below the 10%.
- Based on the developed model, an analysis of the relevance of the melt pool fluid-dynamics in the LMD process has been carried out. Using an exponential formula, this relevance has been quantified, what enables to determine a modeling window where the fluid-dynamic phenomena can be omitted without losing accuracy.
- Thanks to the assumption of no-material movement, computational cost is considerably reduced. Moreover, computational times are ten times lower compared when fluid-dynamics have been considered.

Conflict of interest

The authors declared that there is no conflict of interest.

Acknowledgements

References

[1] S.M. Thompson, L. Bian, N. Shamsaei, A. Yadollahi, An overview of Direct Laser Deposition for additive manufacturing; Part I: transport phenomena, modeling and diagnostics, Addit. Manuf. 8 (2015) 36–62.
[2] G.P. Dinda, A.K. Dasgupta, J. Mazumder, Laser aided direct metal deposition of Inconel 625 superalloy: microstructural evolution and thermal stability, Mater. Sci. Eng. A 509 (2009) 98–104.
[3] E.C. Santos, M. Shiomi, K. Osakada, T. Laoui, Rapid manufacturing of metal components by laser forming, Int. J. Mach. Tools Manuf. 46 (2006) 1459–1468.
[4] E. Toyserkani, A. Khajepour, S. Corbin, Laser Cladding, CRC Press LLC, 2005.
[5] K. Wissenbach, Surface treatment, in: R. Poprawe (Ed.), Tailored Light 2 Laser Application Technology, Springer-Verlag, Berlin Heidelberg, 2011, pp. 173–239 (Chapter 11).
[6] A.J. Pinkerton, Advances in the modeling of laser direct metal deposition, J. Laser Appl. 27 (2015) S15001.
[7] I. Tabernero, A. Lamikiz, S. Martínez, E. Ukar, L.N. López de Lacalle, Geometric modelling of added layers by coaxial laser cladding, Phys. Procedia 39 (2012) 913–920.
[8] W. Ya, B. Pathiraj, S. Liu, 2D modelling of clad geometry and resulting thermal cycles during laser cladding, J. Mater. Process. Technol. 230 (2016) 217–232.

[9] J. Dowden, The Theory of Laser Materials Processing: Heat and Mass Transfer in Modern Technology, Springer Verlag, 2009.

[10] P. Yu, Y. Zeng, Characterization of laser-induced local heating in a substrate, Int. J. Heat Mass Transf. 106 (2017) 989–996.

[11] K. Heller, S. Kessler, F. Dorsch, P. Berger, T. Graf, Analytical description of the surface temperature for the characterization of laser welding processes, Int. J. Heat Mass Transf. 106 (2017) 958–969.

[12] W. Ya, B. Pathiraj, S. Liu, 2D modelling of clad geometry and resulting thermal cycles during laser cladding, J. Mater. Process. Technol. 230 (2016) 217–232.

[13] E. Toyserkani, A. Khajepour, S. Corbin, 3-D finite element modeling of laser cladding by powder injection: effects of laser pulse shaping on the process, Opt. Lasers Eng. 41 (2004) 849–867.

[14] C. Li, C.H. Fu, Y.B. Guo, F.Z. Fang, A multiscale modeling approach for fast prediction of part distortion in selective laser melting, J. Mater. Process. Technol. 229 (2016) 703–712.

[15] I.A. Roberts, C.J. Wang, R. Esterlein, M. Stanford, D.J. Mynors, A three-dimensional finite element analysis of the temperature field during laser melting of metal powders in additive layer manufacturing, Int. J. Mach. Tools Manuf. 49 (2009) 916–923.

[16] H.-L. Dai, Z.-Q. Zheng, W.-L. Xu, H.-B. Liu, A.-H. Luo, Thermoviscoelastic dynamic response for a rectangular steel plate under laser processing, Int. J. Heat Mass Transf. 105 (2017) 24–33.

[17] S. Safdar, A.J. Pinkerton, L. Li, M.A. Sheikh, P.J. Withers, An anisotropic enhanced thermal conductivity approach for modelling laser melt pools for Ni-base super alloys, Appl. Math. Model. 37 (2013) 1187–1195.

[18] Y. Chew, J.H. Lye Pang, G. Bi, B. Bin Song, Thermo-mechanical model for simulating laser cladding induced residual stresses with single and multiple clad beads, J. Mater. Process. Technol. 224 (2015) 89–101.

[19] D. Dai, D. Gu, Influence of thermodynamics within molten pool on migration and distribution state of reinforcement during selective laser melting of AlN/AlSi10Mg composites, Int. J. Mach. Tool Manuf. 100 (2016) 14–24.

[20] Z.S. Saldi, A. Kidess, S. Kenjereš, C. Zhao, I.M. Richardson, C.R. Kleijn, Effect of enhanced heat and mass transport and flow reversal during cool down on weld pool shapes in laser spot welding of steel, Int. J. Heat Mass Transf. 66 (2013) 879–888.

[21] Z. Gan, G. Yu, X. He, et al., Numerical simulation of thermal behavior and multicomponent mass transfer in direct laser deposition of Co-base alloy on steel, Int. J. Heat Mass Transfer 104 (2017) 28–38.

[22] Z. Gan, H. Liu, S. Li, et al., Modeling of thermal behavior and mass transport in multi-layer laser additive manufacturing, Int. J. Heat Mass Transfer 111 (2017) 709–722.

[23] J.M. Flynn, A. Shokrani, S.T. Newman, V. Dhokia, Hybrid additive and subtractive machine tools – research and industrial developments, Int. J. Mach. Tools Manuf. 101 (2016) 79–101.

[24] S.V. Patankar, Numerical Heat Transfer and Fluid Flow, McGraw-Hill Book Company, 1980.

[25] J.I. Arrizubieta, I. Tabernero, J.E. Ruiz, A. Lamikiz, S. Martinez, E. Ukar, Continuous coaxial nozzle design for LMD based on numerical simulation, Phys. Procedia 56 (2014) 429–438.

[26] I. Tabernero, A. Lamikiz, S. Martínez, E. Ukar, L.N. López de Lacalle, Modelling of energy attenuation due to powder flow-laser beam interaction during laser cladding process, J. Mater. Process. Technol. 212 (2012) 516–522.

[27] S. Pang, X. Chen, W. Li, X. Shao, S. Gong, Efficient multiple time scale method for modeling compressible vapor plume dynamics inside transient keyhole during fiber laser welding, Opt. Laser Technol. 77 (2016) 203–214.

[28] G.C. Onwubolu, J.P. Davim, C. Oliveira, A. Cardoso, Prediction of clad angle in laser cladding by powder using response surface methodology and scatter search, Opt. Laser Technol. 39 (2007) 1130–1134.